Observable Signatures of Quarkyonic Phase in Neutron Stars

Probit J Kalita,¹ Tuhin Malik,² Tiangi Zhao,³ Bharat Kumar,^{1,*} and James M. Lattimer⁴

In this letter, we perform Bayesian inference on quarkyonic equation-of-state models and find they remain viable under all current astrophysical constraints. Crucially, we identify a novel observational diagnostic: the slope of the M–R relation at fixed mass versus the central sound speed. Quarkyonic stars occupy a distinct region (high central c_s^2 and positive dR/dM) from purely nucleonic stars. This could be tested by future radius measurements of two stars of different mass. Our results indicate that if a neutron star falls in the quarkyonic region, it would be strong evidence for quarkyonic matter in its core.

Introduction - The composition of neutron stars (NSs), relics of what were once massive stars, and a universal description of matter in the extreme densities inside them remains an elusive mystery. The primary dilemma that we find ourselves in is accommodating two constraints from astronomical observations, the $\gtrsim 2 {\rm M}_{\odot}$ observations of neutron star mass [1, 2], and the compact radii inferred from the binary neutron star merger event GW170817 [3]. As argued by McLerran and Reddy, these require the matter in the NS core to have very high pressures in the deep interior to allow for the high mass, while also requiring the pressure towards the exterior of the core being relatively low which would allow for the high mass to get squished into a $\lesssim 13.5$ km radius. This corresponds to the speed of sound $(c_s = \sqrt{\partial P/\partial \mathcal{E}})$, where Pis pressure and \mathcal{E} is energy density of the matter), the rate at which a perturbation would travel mechanically in the star, increasing rapidly in the core [4, 5].

In quarkyonic matter [6], nucleons emerge as colorsinglet quasiparticles confined to a shell near the Fermi surface [4]. Deep inside the Fermi sea, quarks fill momentum states and dominate the bulk thermodynamics while remaining globally confined [7]. This distinct structure of the Fermi sea arises from the duality between hadronic and quark degrees of freedom [8], naturally resolving the hyperon puzzle [9]. Improvements to the model were made by Zhao and Lattimer, where protons and leptons were incorporated into the system in a manner that ensured the NS matter remains in chemical and beta-equilibrium. This description of NS matter not only allowed for the observational constraints to be satis fied, it also ensured that c_s^2 , after its rapid rise at NS core densities, would decrease to the conformal limit of 1/3 at high densities.

Given this new theoretical framework for generating the NS matter equation of state (EoS), two pertinent questions arise: How well constrained are the model parameters and how well can they be constrained, and can one possibly distinguish NSs with a quarkyonic phase from a completely hadronic NS? To address these ques-

tions, in this letter, we perform a Bayesian inference of the model parameters using multimessenger observations and theoretical calculations as constraints, improving the understanding and accuracy of the model. Using the slope of the mass-radius relation $(\mathrm{d}R/\mathrm{d}M)$, which has been used to point towards potential signatures of hyperons in NSs [11, 12], analysis of our results show that $\mathrm{d}R/\mathrm{d}M$ and c_s^2 have distinguishable change in distribution when the quarkyonic phase appears, and use of these two along with the NS radius give us indicators that can be used to identify the presence of a quarkyonic phase in the star.

Methods - Identifying all the parameters in the model (refer to [10] for details) which are not fixed, either theoretically or experimentally, gives us seven quantities that the EoS is sensitive to. These model parameters along with the possible ranges in which they can vary are listed in Table I.

TABLE I. The model parameters and their priors utilized for the Bayesian inference. These priors are either set as Gaussian priors for parameters which have experimentally obtained values, and uniform priors for the remaining parameters. $\rho_0 = 0.16 \ \mathrm{fm}^{-3}$ is the nuclear saturation density.

Model Parameter	Prior type	Range
Quarkyonic transition density (ρ_t) (fm ⁻³)	Uniform	[0.18, 0.8]
QCD scale parameter Λ_{qcd} (MeV) [10]	Uniform	[10, 2000]
Symmetry energy at ρ_0 (J) (MeV) [13]	Gaussian	32.5 ± 2.5
Slope of symmetry energy at ρ_0 (L) (MeV)	Uniform	[20, 100]
Incompressibility at ρ_0 (K) (MeV) [13]	Gaussian	230 ± 40
Binding energy at ρ_0 (BE/A) (MeV) [13]	Gaussian	16 ± 0.2
γ_1 term in interaction potential [10]	Uniform	[0.5, 5.0]

 $^{^{\}rm a}$ listed as (mean \pm standard deviation)

Following the Bayesian inference framework developed in Ref. [14–17], we use Bayes' theorem to calculate the posterior distribution of the model parameters, and this seven-dimensional parameter space is traversed via nested sampling using the UltraNest package [18]. Obtaining the Bayes' probability for each parameter vector involves evaluating the likelihood of how well the NSs de-

¹Department of Physics & Astronomy, National Institute of Technology, Rourkela 769008, India ²CFisUC, Department of Physics, University of Coimbra, PT 3004-516 Coimbra, Portugal ³University of California, Berkeley, CA 94720, U.S.A.

⁴Department of Physics & Astronomy, Stony Brook University, Stony Brook, NY 11794, U.S.A. (Dated: October 28, 2025)

^b listed as the closed range [lower limit, upper limit]

scribed by it agree with multimessenger observations and theoretical bounds, and which is how we impose the requirement for the results to satisfy those bounds. We do this thrice to get three constrained sets from the Bayesian inference process, Sets- α , β and γ . For Set- α , we use pulsar mass and radius measurements from NICER for PSR J0030+0451 [19] and PSR J0740+6620 [20], the mass and tidal deformability measurements from LIGO/Virgo for the binary neutron star merger event GW170817 [3], and ab-initio low-density nuclear theory bounds on EoS from χ EFT calculations given by Huth et al. [21], imposed up to the nuclear saturation density, $\rho_0 = 0.16 \text{ fm}^{-3}$. In Set- β we expand the number of bounds by including the two recently reported NICER measurements of PSR J0437-4715 [22] and PSR J0614-3329 [23], and set a ceiling on the maximum mass at $M_{\text{max}} \leq 2.33 \text{ M}_{\odot}^{-1}$ [24]. In Set- γ , we place a stricter maximum mass limit of $M_{\rm max} \leq 2.15 {\rm M}_{\odot}$, based on Ref. [25]². We also ensure that each EoS remains causal ($c_s^2 \leq 1$ at all densities), and that every EoS is able to produce a NS of mass 1.97 M_{\odot} [1]³. The increasing requirements to be satisfied causes the final parameter space of the three sets to get progressively more constrained.

Each parameter set for each final constrained set (α, β, γ) gives an EoS describing the pressure-energy density relation in NS matter, and these EoSs are used to compute the structure by solving the Tolman–Oppenheimer–Volkoff equations [26–29], yielding the mass–radius, and mass–tidal deformability relations for each set. In what follows we describe the resulting posteriors and the novel diagnostics extracted from them.

Results - Figure 1 presents the results of the Bayesian inference as a correlation corner-plot of the seven model parameters, with their posterior distributions being shown in the diagonal sub-figures. ρ_t , which determines the density for quarkyonic transition, can be seen to have a distribution which is not entirely Gaussian as it reverts to a uniform distribution at higher density values. The location of where the peak of the Gaussian region lies shifts to higher densities and its width broadens as we go from Set- α towards Set- γ . Physically, imposing a limit of a lower allowed maximum mass means that we allow the stars in Sets β and γ to have relatively lower pressures in the inner NS core than Set- α , allowing ρ_t to be higher as quarks are not required until then. The Gaussian tail morphing into a uniform distribution implies that models with low (to negligible) quark content at stellar densities

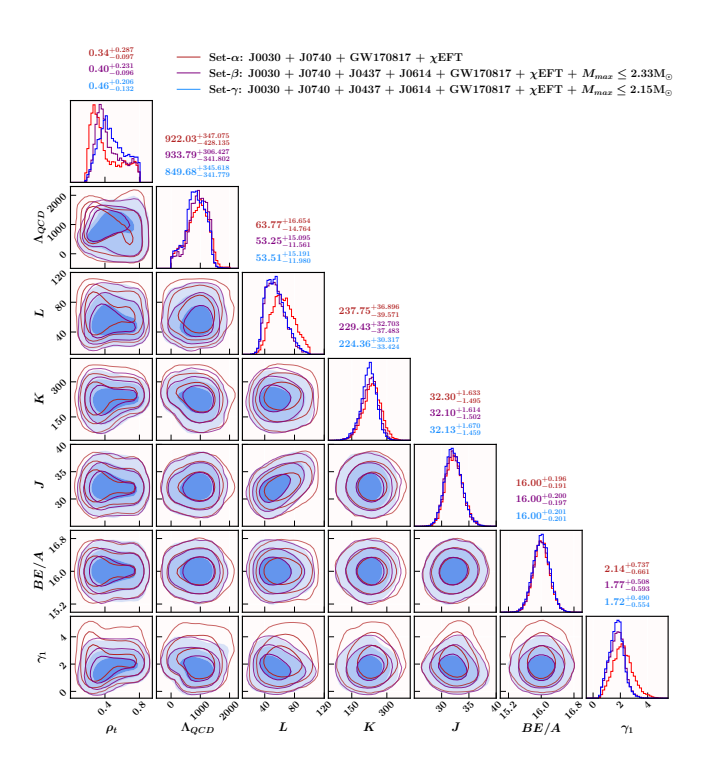


FIG. 1. Correlation corner-plot between the seven parameters of the quarkyonic matter model showing the Bayesian inference results at the 1σ , 2σ and 3σ levels. The diagonal members show the posterior distribution histogram of the parameters, with its constrained value listed above the histograms. The results for Set- α , β and γ are represented using the colors red, purple, and blue, respectively.

are still able to satisfy the current astronomical bounds, which are thus insufficient to fully constrain the value of ρ_t . The posteriors for $\Lambda_{\rm QCD}$, L, K and γ_1 are also observed to be significantly narrowed through the inference process. Particularly, the symmetry energy slope's (L) posterior shrinks in width and shifts to a lower value when the newer constraints in Sets β and γ get imposed, reflecting the effectiveness of the use of astronomical observations in augmenting terrestrial nuclear experiments with the aim of a better understanding of dense matter.

The outcome of the Bayesian inference is better understood via Fig. 2, where we show the posterior distributions of the NS pressure-energy density, mass-radius and mass-tidal deformability relations. The EoS plot in Fig. 2a shows the 1-dimensional posterior distribution of pressure (P) on a grid of energy density (\mathcal{E}) . The regions bounded by the solid red line, dashed purple line, and dashed blue line (with blue dotted interior) denote the 90% confidence limits of the posteriors from Sets α , β and γ , respectively. Bounds on the EoS had been given by Annala et al., where they had utilized a speed-of-sound interpolation method to generate EoSs satisfying the $M \geq 1.97~\mathrm{M}_\odot$ and $70 < \Lambda_{1.4} < 580$ constraints, and the region of the $P - \mathcal{E}$ space occupied by the causally

 $^{^1}$ using the 1σ upper bound value from the maximum mass limit of $2.25^{+0.08}_{-0.07}~\rm M_\odot$ given by Fan <code>et al.</code>

 $^{^2}$ we take a slightly lower mass limit than the reported 2.17 \pm 0.09 M_{\odot} in Ref. [25] as the aim is to study the impact a more stringent mass limit will have

³ such that each parameter set is able to explain the heaviest observed NSs

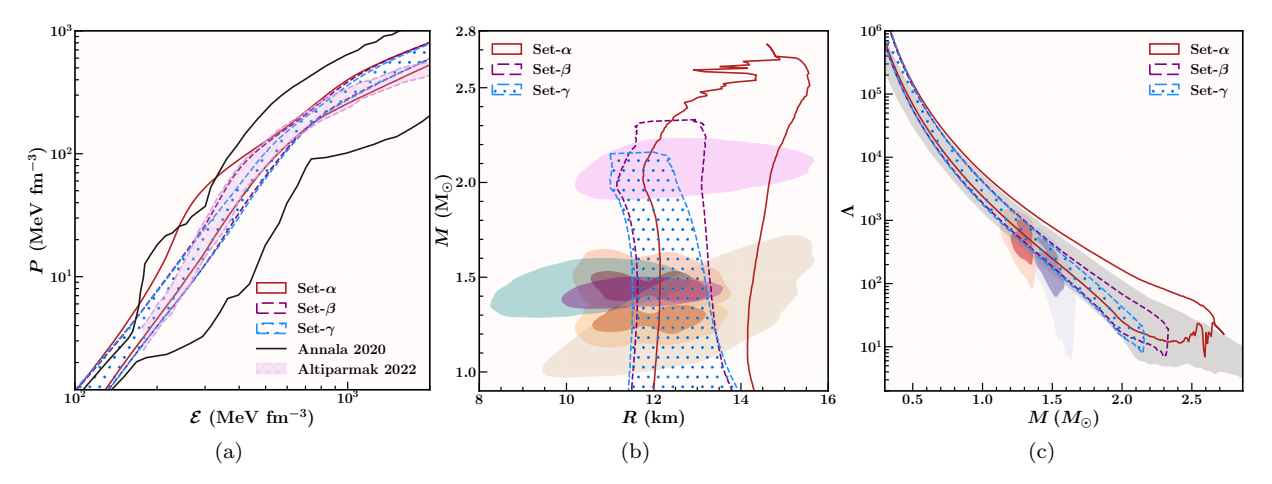


FIG. 2. The 1-dimensional posterior distributions, at the 90% confidence interval, of (a) pressure on an energy density grid, (b) radius on a mass grid, and (c) dimensionless tidal deformability on a mass grid, for the three resulting sets of parameter values α , β , and γ - represented by the solid red boundary, dashed purple boundary, and dashed blue boundary with blue dotted interior, respectively. The solid black lines and the salmon shaded region in (a) show bounds on EoS given in Ref. [30, 31]. The 2σ bounds on the mass-radius plane from NICER observations are shown in (b) with the tan (PSR J0030+0451) [19], salmon (PSR J0740+6620) [20], teal (PSR J0437-4715) [22], and violet (PSR J0614-3329) [23] patches, while the light/dark orange shaded regions are the 90% and 50% bounds from GW170817 [3]. The grey shaded region in (c) is the 90% CI region for full $M-\Lambda$ posterior from GW170817 [32], while the red and purple regions denote the 90% (light) and 50% (dark) bounds on the observed values in GW170817 [3].

allowed $(c_s^2 \le 1)$ EoSs is demarcated by the solid black lines [30]. The salmon shaded area corresponds to the region where EoSs are most likely to be found in, as identified by Altiparmak et al. using a similar speed-of-sound based approach [31]. Fig. 2b shows the 1-dimensional posterior distribution of the stellar radius (R) on a grid of the stellar mass (M) using the same color scheme as Fig. 2a. The patches correspond to bounds on mass and radius from astronomical observations, with the regions in tan, salmon, teal and violet marking the 2σ confidence intervals of the pulsars PSR J0030+0451 [19], PSR J0740+6620 [20], PSR J0437-4715 [22], and PSR J0614-3329 [23], respectively. The light and dark orange patches correspond to the 50% and 90% CI regions of the binary components of GW170817 [3]. And Fig. 2c shows the 1-dimensional posterior distribution of the dimensionless tidal deformability (Λ) on a grid of the stellar mass (M) obtained using the formalism given in Ref. [28, 29]. Similar to the figures to its left, it marks the data from Sets α , β and γ in red, purple and blue respectively. The red and purple patches denote the 50% and 90% CI region for the lighter and heavier counterparts of GW170817 [3]. The grey shaded region is the 90% credible level of the full $M-\Lambda$ posterior from GW170817 obtained from parametric EoSs [32, 33]. As the limitations on the mass, radius and tidal deformability are increased going from Set- α to γ , the posterior distributions are also seen to shrink and leading to better fits with the observational bounds. As expected from Set- α , it has the widest posterior regions due to not having to satisfy that many constraints, while

Set- γ does not differ from Set- β by much due to only the maximum mass limit being changed. It is worth noting that the pressure posterior of Set- α has a significant hump in the $\sim 200-400 \text{MeV}$ region which is absent from the other two (and also extends beyond the EoS bounds shown in black), indicating that it is this sharp pressure increase which allowed for the high masses and large radii achieved by this set. Annala et al. had imposed strict bounds on $\Lambda_{1.4}$ which were not imposed during our inference process, and with no small radii observations to motivate Set- α to yield NSs with higher compactness, we get the wide posteriors of P, R and $\Lambda_{1.4}$. Sets β and γ having two low radii observations to satisfy end up in a situation analogous to the tight $\Lambda_{1,4}$ constraints of Ref. [30], leading to their pressure posteriors staying inside the black lines.

The distinction of neutron stars based on their makeup is a challenge which is being explored actively, and the slope of the M-R relation has emerged as a promising candidate for addressing the problem [11, 12, 34]⁴. The M-R relation is a reflection of the EoS of the NS matter, and its slope maps the stiffness of the EoS [11]. These works attempt to address detection of hyperons in NSs [11, 12] or Maxwell-type first-order phase transition to quark matter [34]. Observational estimates of

⁴ Tang et al. use the finite difference $\Delta R = R_{1.4} - R_2$ in their work instead of the derivative, but both can be used interchangeably due to their strong positive correlation.

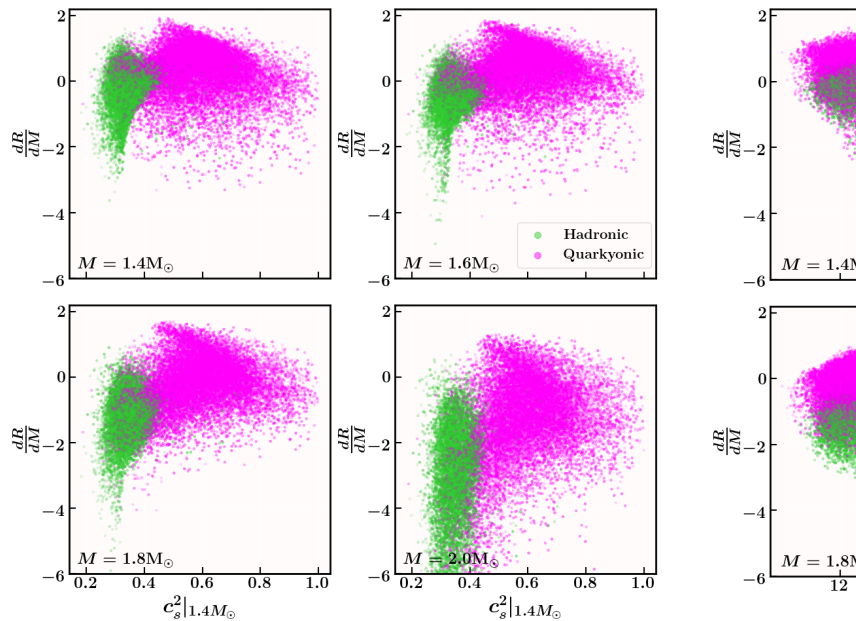


FIG. 3. Differentiation between hadronic composition and presence of a quarkyonic phase in canonical NSs as seen by the distinct separation when the slope of the R-M curve at different stellar masses is plotted as a function of the speed of sound at the center of the canonical mass neutron star. The color of the dots represent if the canonical NS's composition is hadronic (green) or if a quarkyonic phase appears (magenta). The mass at which the slope of the R-M curve is taken at is noted in the lower-left corner of each sub-figure.

dM/dR at specific masses have also been shown to potentially constrain nuclear matter properties [11, 34].

To determine the presence of a quarkyonic phase inside a canonical mass neutron star $(M = 1.4 \text{ M}_{\odot})$ we make use of the slope of the M-R relation, the c_s^2 at the center of the NS, and the radius of the star. Physically, the slope dR/dM^5 reflects how quickly the star's size changes with mass is added to it, while c_s^2 encodes the rate at which the pressure inside the core increases. Computing the derivative $\frac{dR}{dM}|_{M^*}$ at a fixed mass $M^* = 1.4, 1.6, 1.8, 2.0 M_{\odot}$, for every parameter set of all the three Sets- α , β and γ , we plot this slope against the square of the speed of sound at the center of the 1.4 M_{\odot} NS, $c_s^2(r=0)$, in Fig. 3. A clearly visible separation is observed between NSs of hadronic composition (green) and those with a quarkyonic phase (magenta) with the former being present in the limited range of $c_s^2 \sim 0.2$ to ~ 0.4 , while the latter category of NSs have higher central c_s^2 , thus each occupying a distinct region in the $dR/dM - c_s^2$ plane. This distinction arises due to quarks aiding in the rapid increase

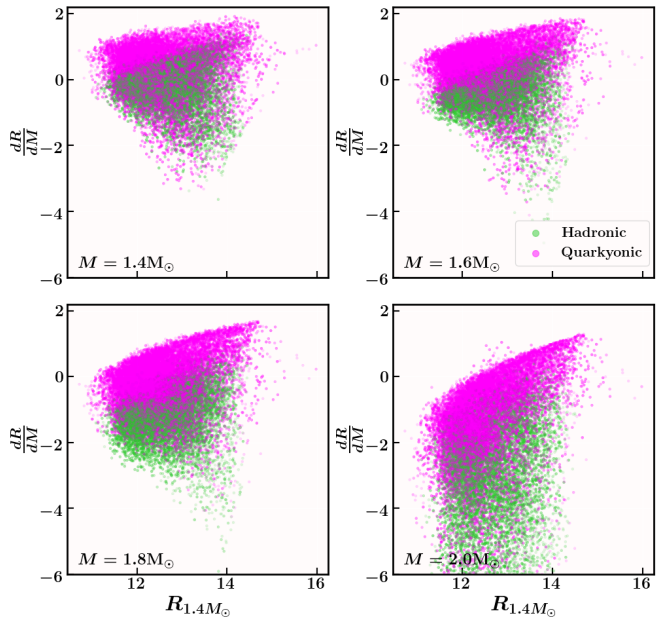


FIG. 4. Differentiation between hadronic composition and presence of a quarkyonic phase in canonical NSs shown by the separation when the slope of the R-M curve at different stellar masses is plotted as a function of the radius of the canonical mass neutron star. The color of the dots represent if the canonical NS's composition is hadronic (green) or if a quarkyonic phase appears (magenta). The mass at which the slope of the R-M curve is taken at is noted in the lower-left corner of each sub-figure.

in speed of sound — in NSs which are fully hadronic, the EoS up to the central density of $\rho_c = \rho(r=0)$, have not been stiffened by quarks $(\rho_c \leq \rho_t)$ and thus the c_s^2 remains near the conformal limit, but in quarkyonic NSs the quarks appear before the central density has been reached $(\rho_c \geq \rho_t)$, causing c_s^2 to shoot up and thus occupy a region above the conformal limit. In other words, for a given increase in central pressure the radius response is altered. Since the EoSs of the hadronic stars are not affected by quarks due to them not appearing anywhere below the star's central density, hadronic stars obtained from any formalism used to describe NS matter would still occupy the same region as in our case, thus meaning that the observation of a NS in the magenta region would be an evidence in the favor of a quarkyonic or quarkyonic-like phase in the star.

The $c_s^2(r=0)$ is, however, not a directly measurable property and needs to be inferred via indirect means from gravitational waves via asteroseismological techniques. Radius on the other hand is a much more easily measurable quantity, and it too is seen to provide a good means of distinguishing between NS compositions in Fig. 4. The derivative is here plotted against the canonical mass NS's radius $(R_{1.4})$, and we see that quarkyonic stars tend to

⁵ We use the slope of the R(M) relation instead of the M(R) relation as it circumvents the issue of the derivatives becoming infinite, as has been pointed out in Ref. [12].

have a positive value of the slope while preferring smaller radii, while hadronic stars tend to have a negative value of the slope. This difference in behaviour comes from the transition to quarkyonic matter making the NS core much stiffer, which means that its radius increases (or if it decreases then it does so at a slower rate) when mass gets added to it. This makes the distribution of $\frac{\mathrm{d}R}{\mathrm{d}M}|_{M^*}$ of canonical NS a good indicator of the star's internal composition.

Crucially, this proposed diagnostic is testable: given precise measurements of the radii of two stars with different masses, one can estimate dR/dM and compare to the predicted c_s^2 (which may be inferred indirectly via observables like the tidal deformability) and the canonical NS radius $R_{1.4}$. If a neutron star falls in the quarkyonic region of the diagnostic plot, it would be evidence in favor of quarkyonic or quarkyonic-like phase being present. To our knowledge, this idea of using the M–R slope against sound speed as an indicator is entirely new and provides a concrete observational handle on neutron-star core composition beyond the usual mass or radius alone.

Discussions and Conclusion - We demonstrate that quarkyonic equations of state can accommodate all current neutron-star constraints while offering unique observable signatures. Our Bayesian analysis shows that even with the inclusion of all recent NICER, LIGO/Virgo and theoretical bounds, quarkyonic EoSs remain viable. Most importantly, we identify the slope of the mass-radius relation at a given mass versus the central sound speed as a powerful diagnostic: quarkyoniccore stars and purely nucleonic stars separate cleanly in this space. This result opens a new window for testing the core composition of neutron stars. Upcoming measurements (for example, continued NICER observations, more precise radio pulsar mass-radius determinations, or further tidal constraints from the next binary-merger detections) can refine these diagnostics. A measurement of the predicted mass-radius slope and sound speed for neutron stars could thus provide the first direct evidence for or against the presence of quarkyonic or quarkyonic-like phase in their cores.

Acknowledgement - PJK and BK acknowledge the usage of IUCAA HPC computing facility under project ID hpc2502001. JML acknowledges funding from the US Department of Energy under Grant DE-FG02-87ER40317.

* kumarbh@nitrkl.ac.in

- P. B. Demorest, T. Pennucci, S. M. Ransom, M. S. E. Roberts, and J. W. T. Hessels, Nature 467, 1081 (2010).
- [2] J. Antoniadis et al., Science **340**, 6131 (2013).
- [3] B. Abbott et al., Phys. Rev. Lett. **121**, 161101 (2018).
- [4] L. McLerran and S. Reddy, Phys. Rev. Lett. 122, 122701 (2019).

- [5] I. Tews, J. Carlson, S. Gandolfi, and S. Reddy, Astrophys. J. 860, 149 (2018).
- [6] L. McLerran and R. D. Pisarski, Nucl. Phys. A 796, 83 (2007).
- [7] Y. Hidaka, L. D. McLerran, and R. D. Pisarski, Nucl. Phys. A 808, 117 (2008).
- [8] Y. Fujimoto, T. Kojo, and L. D. McLerran, Phys. Rev. Lett. 132, 112701 (2024).
- [9] Y. Fujimoto, T. Kojo, and L. McLerran, Quarkyonic matter pieces together the hyperon puzzle (2024).
- [10] T. Zhao and J. M. Lattimer, Phys. Rev. D 102, 023021 (2020).
- [11] M. Ferreira and C. Providência, Identifying hyperons in neutron star matter from the slope of the mass-radius diagram (2025).
- [12] A. Bauswein, A. Nikolaidis, G. Lioutas, H. Kochankovski, P. Char, C. Mondal, M. Oertel, L. Tolos, N. Chamel, and S. Goriely, Stellar properties indicating the presence of hyperons in neutron stars (2025).
- [13] J. Cartaxo, C. Huang, T. Malik, S. Sourav, W.-L. Yuan, T. Zhou, X. Liu, and C. Providência, A Complete Survey from the *CompactObject* Perspective on Equation of State Cross-Comparison Using Observational and Nuclear Experimental Constraints (2025).
- [14] S. K. Greif, G. Raaijmakers, K. Hebeler, A. Schwenk, and A. L. Watts, Mon. Not. Roy. Astron. Soc. 485, 5363 (2019).
- [15] G. Raaijmakers et al., Astrophys. J. Lett. **893**, L21 (2020).
- [16] G. Raaijmakers et al., Astrophys. J. Lett. **887**, L22 (2019).
- [17] G. Raaijmakers, S. K. Greif, K. Hebeler, T. Hinderer, S. Nissanke, A. Schwenk, T. E. Riley, A. L. Watts, J. M. Lattimer, and W. C. G. Ho, Astrophys. J. Lett. 918, L29 (2021)
- [18] J. Buchner, JOSS 6, 3001 (2021).
- [19] T. E. Riley et al., Astrophys. J. Lett. 887, L21 (2019).
- [20] T. E. Riley et al., Astrophys. J. Lett. 918, L27 (2021).
- [21] S. Huth et al., Nature **606**, 276 (2022).
- [22] D. Choudhury et al., Astrophys. J. Lett. **971**, L20 (2024).
- [23] L. Mauviard et al., A NICER view of the 1.4 solar-mass edge-on pulsar PSR J0614–3329 (2025).
- [24] Y.-Z. Fan, M.-Z. Han, J.-L. Jiang, D.-S. Shao, and S.-P. Tang, Phys. Rev. D 109, 043052 (2024).
- [25] D.-S. Shao, S.-P. Tang, X. Sheng, J.-L. Jiang, Y.-Z. Wang, Z.-P. Jin, Y.-Z. Fan, and D.-M. Wei, Phys. Rev. D 101, 063029 (2020).
- [26] R. C. Tolman, Phys. Rev. **55**, 364 (1939).
- [27] J. R. Oppenheimer and G. M. Volkoff, Phys. Rev. **55**, 374 (1939).
- [28] T. Hinderer, Astrophys. J. 677, 1216 (2008).
- [29] T. Hinderer, B. D. Lackey, R. N. Lang, and J. S. Read, Phys. Rev. D 81, 123016 (2010).
- [30] E. Annala, T. Gorda, A. Kurkela, J. Nättilä, and A. Vuorinen, arXiv:1903.09121 [astro-ph.HE] 16, 907 (2020).
- [31] S. Altiparmak, C. Ecker, and L. Rezzolla, Astrophys. J. Lett. 939, L34 (2022).
- [32] LIGO-P1800115-v12: GW170817: Measurements of Neutron Star Radii and Equation of State.
- [33] B. Abbott et al., Phys. Rev. X 9, 011001 (2019).
- [34] S.-P. Tang, Y.-J. Huang, and Y.-Z. Fan, Physical Review D 112, 083009 (2025).